Title

Evolution of the Fermi surface of Weyl semimetals in the transition metal pnictide family

Journal

Nature Materials, 15(1)

ISSN

1476-1122

Authors

Liu, ZK

Yang, LX

Sun, Y

et al.

Publication Date

2016

DOI

10.1038/nmat4457

Peer reviewed

Fermiology Evolution of Weyl Semimetals in Transition Metal Pnictide Family

Z. K. Liu[1,2†], L. X. Yang[3,4,5†], Y. Sun[6†], T. Zhang[3,4], H. Peng[4], H. F. Yang[4,7], C. Chen[4], Y. Zhang[5], Y. F. Guo[4], D. Prabhakaran[4], M. Schmidt[6], Z. Hussain[5], S.-K. Mo[5], C. Felser[6], B. Yan[1,6] and Y. L. Chen[4,1,2,3]

[1]*School of Physical Science and Technology, ShanghaiTech University, Shanghai 200031, China*
[2]*Diamond Light Source, Didcot, Oxfordshire, OX11 0QX, UK*
[3]*State Key Laboratory of Low Dimensional Quantum Physics, Collaborative Innovation Center of Quantum Matter and Department of Physics, Tsinghua University, Beijing 100084, P. R. China*
[4]*Physics Department, Oxford University, Oxford, OX1 3PU, UK*
[5]*Advanced Light Source, Lawrence Berkeley National Laboratory, Berkeley, CA 94720, USA*
[6]*Max Planck Institute for Chemical Physics of Solids, D-01187 Dresden, Germany*
[7]*State Key Laboratory of Functional Materials for Informatics, SIMIT, Chinese Academy of Sciences, Shanghai 200050, China*

† *These authors contributed equally to this work*
* *Email: yulin.chen@physics.ox.ac.uk*

The discovery of quantum materials with non-trivial topological electronic structures has recently ignited worldwide interest in physics and materials science[1,2]. Topological Weyl semimetals (TWSs) represent a novel state of topological quantum matter[3-6] which not only possesses Weyl fermions (intriguing massless chiral particles that can be viewed as magnetic monopoles in momentum space) in the bulk and unique Fermi-arcs generated by topological surface states, but also exhibits appealing physical properties such as extremely large magnetoresistance and ultra-high carrier mobility[7-10]. Here, by performing angle-resolved photoemission spectroscopy (ARPES) on NbP and TaP, we directly observed their band structures with characteristic Fermi-arcs of TWSs. Additionally, by systematically investigating NbP, TaP and TaAs from the same transition metal monopnictide family, we discovered their Fermiology evolution with spin-orbit coupling (SOC) strength. Our experimental findings not only reveal the mechanism to realize and fine-tune the electronic structures of TWSs, but also provide a rich material base for exploring many exotic physical phenomena (e.g. chiral magnetic effects, negative magnetoresistance, and quantum anomalous Hall effect) and novel future applications[5,6,11-13].

Three-dimensional (3D) topological Weyl semimetals (TWSs) represent a new state of quantum matter recently proposed with unusual electronic structures that resemble both a "3D graphene" and a topological insulator (TI). On one hand, a TWS possesses the bulk Weyl fermion, a unique chiral particle which disperses linearly along all three momentum directions across a point – the Weyl point which can be viewed as a magnetic monopole in momentum space[14]. As a Weyl fermion contains half of the degrees of freedom of a Dirac fermion, they always appear in pair (with opposite chirality) in materials[3,5,6,14]. On the other hand, a TWS also possesses non-trivial topological surface states that form unique "Fermi-arcs" [3,5,6]– unusual Fermi surfaces (FSs) consisting of unclosed curves that start and end at Weyl points (Fig. 1b). The unusual bulk and surface electronic structure of 3D TWSs can give rise to many exotic phenomena, such as negative magnetoresistance, chiral magnetic effects, quantum anomalous Hall effect, novel quantum oscillations (in magneto-transport) and quantum interference (in tunneling spectroscopy)[12,15-18]. In addition, appealing transport properties have also been discovered in some 3D TWS candidates, such as the ultra-high carrier mobility and extremely large magnetoresistance[7-10], making 3D TWSs not only ideal for fundamental research, but also promising materials for novel applications.

Comparing to 3D topological Dirac semimetals (TDSs)[19-22] which possess bulk Dirac fermions, 3D TWSs can be realized by breaking either the time reversal symmetry (TRS) or inversion symmetry in 3D TDSs[3-5,23,24] – thus a Dirac point can be split into a pair of Weyl points of opposite chirality. In the past few years, several compounds (e.g. $Y_2Ir_2O_7$[3] and $HgCr_2Se_4$[4]) have been proposed to be TWS candidates with spontaneously broken TRS. Unfortunately, none have been experimentally confirmed up to date.

On the other hand, recent theoretical investigations[5,6,24] pointed out that various compounds with spontaneously broken inversion symmetry can also be TWS candidates, with a promising family of transition metal monopnictides (including NbP, NbAs, TaP and TaAs) [5,6]. In this family of materials, a total of twelve pairs of Weyl points are predicted to exist within a 3D Brillouin Zone (BZ), with each pair residing across one of the two crystalline

mirror planes (Fig. 1a) and being connected by the unique surface Fermi-arcs (Fig. 1b). In the formation of the TWS, the spin-orbit coupling (SOC) plays an essential role and the splitting between the Weyl points and the Fermi-arcs should increase with the strength of the SOC in different compounds (Fig. 1b)[5], which is confirmed by our *ab initio* calculations (Fig. 1c).

In this work, we first investigated the electronic structure of TWS candidates NbP and TaP by ARPES and observed the characteristic surface Fermi-arcs in both compounds. The excellent agreement between our experiments and *ab initio* calculations (as well as other theoretical investigations[5,6]) confirmed that NbP and TaP are TWSs. More importantly, we systematically studied the evolution of the band structures of NbP, TaP and another compound, TaAs in the same family (which was recently confirmed as TWS[7,9,25,26]) and discovered clear increase of the separation between the Weyl points and Fermi-arcs from NbP to TaP, and to TaAs. Our result for the first time demonstrates the crucial effect of the SOC in the formation and fine-tuning of the electronic structure of TWSs, including the Fermi arc splitting and Weyl point separation – which will facilitate the designing of new TWS materials with tailored electronic properties.

The crystal structure of NbP and TaP are illustrated in Fig. 1d, which have the same crystal symmetry but slightly different lattice constants (NbP: a=b= 3.33 Å, c = 11.37 Å, TaP: a=b=3.33 Å, c=11.39 Å). Taking NbP as an example, its tetragonal unit cell is formed by four NbP layers with repeating ... –NbP_1-NbP_2-NbP_3-NbP_4–… stacking sequence without inversion symmetry (Fig. 1d)[27]. As the inter-layer distance between the Nb and P planes along *c*-direction (0.167*c* /1.899Å) is about twice as large as their intra-layer distance (0.083*c*/0.944Å), the crystal can be naturally cleaved between adjacent NbP layers (Fig. 1d and Fig. S1 in Supplementary Information) for the ARPES measurements [Fig. 1e(i)]. The high quality of the NbP crystals is verified by the sharp X-ray diffraction patterns from all three crystalline orientations (Fig. 1e(ii-iv)), and the core-level photoemission spectrum (Fig. 1f), which clearly indicates different characteristic Nb (*4s, 4p, 3d*) and P (*2s, 2p)* peaks. The overall electronic structure of NbP is captured in Fig. 1g by a broad momentum space mapping, which shows the global FS topology across multiple Brillouin zones (BZs) of the

(001) surface that agrees excellently with our *ab initio* calculations (overlapped dotted plots). The Fermi surface is comprised of two cross-shape FSs centered at the $\bar{X}$ and $\bar{Y}$ points, each containing two sets of orthogonal FS pockets: the spoon-like and the bowtie-like pockets marked as α-FS and β-FS in Fig. 1g, respectively. As the broken Nb-P bonds are along orthogonal directions between adjacent cleaved NbP layers (see Fig. S1 in Supplementary Information for details), ARPES measurements sometimes show electronic structures from both kinds of layers (Fig. 1h, also see Fig. S1-S2 in Supplementary Information for more discussion).

In Fig. 2, we illustrate the detailed electronic structure of NbP. The stacking plots of constant energy contours at different binding energies (Fig. 2a) show the electronic structure evolution from the isolated cross-shape FSs centered at the $\bar{X}$ and $\bar{Y}$ points to more complicated interconnected texture at higher binding energies. To compare with the *ab initio* calculations, in Fig. 2b we present three side-by-side comparison examples which demonstrate broad agreement: both the spoon-like and bowtie-like FS pockets [Fig 2b (i)] and their evolution to nested textures at higher binding energies [Fig. 2b (ii) and (iii)] can be nicely reproduced by the calculation. Remarkably, the characteristic Fermi-arc type FS suggested by our *ab initio* calculation and previous theoretical investigations[5,6] clearly shows up as the spoon-like FSs, as we will discuss in details in Fig. 4 later.

In addition to the Fermiology and constant energy contours, the band structure for both the spoon and bowtie-like FSs with overlaid dispersions from calculation are presented as 3D plot in Fig. 2c, which again shows excellent agreement. In fact, the overall agreement between experiment and theory can be seen throughout the whole BZ, as illustrated by the comparison in Fig. 2d. Finally, to verify the surface nature of the spoon and bowtie-like FSs (as suggested by our *ab initio* calculations and ref [5,6]), we carried out photon energy dependent ARPES measurements[28] to investigate the k_z dispersion of these bands. In Fig. 2e, the ARPES spectra over a broad photon energy range (52–130 eV) clearly demonstrate the lacking of vertical dispersions (i.e. no k_z-dispersion, more information of photon energy

dependent measurements can be found in the Supplementary Information), proving their surface nature (the photon energy dependent measurement along both $\bar{\Gamma} - \bar{X}$ and $\bar{\Gamma} - \bar{Y}$ directions can be found in the Supplementary Information).

Similar measurements were also conducted on another member (TaP) of the same family of compounds. As can be seen in Fig. 3, the overall electronic structure, such as the FS topology, including the spoon-like and bowtie-like FS pockets (Fig. 3a, b), and the band dispersions along different directions (Fig. 3c, d), again shows excellent agreement with the *ab initio* calculations. The difference between the measured band structure of TaP (Fig. 3) and NbP (Fig. 2) is mainly quantitative: the bands that generate the spoon-like FS have larger splitting in TaP (as will be discussed later with Fig. 4).

The existence of Fermi-arcs on the surface of TaP can also be verified by counting the number of FS crossings along a closed reference loop in the BZ[26] and get an odd number of FS crossings (Fig. 3d). As shown in Fig. 3e, along the closed loop of $\bar{\Gamma} - \bar{X} - \bar{M} - \bar{\Gamma}$, we observe 7 (an odd number) FS crossings in total, which confirms the existence of the Fermi-arcs (more discussions and counting of FS crossings in NbP can be found in the Supplementary Information). In addition to the unique surface Fermi-arc, we also carried out ARPES measurements with high photon energy to investigate the bulk Weyl fermion in TaP (see Supplementary Information).

After establishing the experimental band structures of NbP and TaP, we now focus on the characteristic spoon-like FS, which forms the Fermi-arcs that connect the two Weyl points of opposite chirality as suggested by recent theoretical investigations[5,6] and our calculations [see Fig. 4a(i)]. To investigate the evolution of Fermi-arcs over different compounds in this transition metal monopnictide family, we also carried out ARPES experiments on TaAs (more details can be found in the Supplementary Information) in addition to NbP and TaP.

Measurements with high momentum and energy resolution on the spoon-like FSs for all three compounds are summarized in Fig. 4 – which can be nicely reproduced by our calculations (Fig. 4a), including each FS piece and its detailed shape, thus confirming the

three compounds are TWSs as proposed[5]. The detailed FS topology and associated band dispersions are illustrated in Fig. 4b-d, indicating clear increase of the separation between the Weyl points [ΔK1 in panel (i) and (ii) of Fig. 4b-d] and the Fermi-arcs [ΔK2 in panel (i) and (iii) of Fig. 4b-d] from compound NbP to TaP and to TaAs. In Fig. 4e we assemble the ΔK1 and ΔK2 values extracted and plot them against the SOC strength of the three compounds, which clearly verifies their correspondence and showing that the SOC can act as an effective controlling parameter to tune the splitting of the Weyl points and Fermi-arcs (more discussions can be found in the Supplementary Information).

Our systematic study on the electronic band structures of NbP, TaP and TaAs and observation of the characteristic surface Fermi-arcs, together with the excellent agreement with the theoretical prediction[5,6] and our detailed *ab initio* calculations establish the first TWS family in transition metal monopnictides. This discovery and the SOC controlled band structure and Fermiology tuning further pave the way for the exploration of novel phenomena and potential future applications in TWSs.

Methods:

Sample synthesis:

Single crystals of NbP and TaP of high quality were grown via chemical transport reaction using iodine as transport agent. The compounds NbP have first been synthesized by a direct reaction of the elements niobium (Chempur 99.9%) and red phosphorus (Heraeus 99.999%) at 800 °C in evacuated fused silica tubes for 48 hours. Starting from this microcrystalline powder, NbP crystallized by a chemical transport reaction in a temperature gradient from 850 °C (source) to 950 °C (sink), and a transport agent concentration of 13.5 mg/cm^3 iodine (Alfa Aesar 99.998%). TaP is prepared using elements tantalum (Alfa Aeser 99.9%) and red phosphorus (Heraeus 99.999%) using the same method as NbP.

Precursor polycrystalline TaAs samples were prepared by mixing high purity (>99.99%) Ta and As elements and the mixture were sealed into a quartz tube under high vacuum, which was sealed into another evacuated tube for extra protection. First, the vessel

was heated to 600°C at a rate of 50°C/hour, after 10 hours of soaking, it was slowly heated to 1050°C at 30°C/hour rate and kept at this temperature for 24 hours. Finally the vessel was cooled down to room temperature.

With the polycrystalline precursor, the single crystals were grown using chemical vapor transport method in a two zone furnace. The polycrystalline TaAs powder and 0.46 mg/cm^3 of Iodine was loaded into a 24mm diameter quartz tube and sealed under a vacuum. The charge part of the tube was kept at 1150°C and the other end at 1000°C for three weeks. The resulting crystals can be as large as 0.5-1mm in size.

Angle resolved photoemission spectroscopy:

ARPES measurements were performed at beamline 10.0.1 of the Advanced Light Source (ALS) at Lawrence Berkeley National Laboratory, USA and beamline I05 of the Diamond Light Source (DLS), UK. The measurement pressure was kept below $3\times10^{-11}/1.5\times10^{-10}$ Torr in ALS/DLS, and data were recorded by Scienta R4000 analyzers at 10K sample temperature at both facilities. The total convolved energy and angle resolutions were 16meV/30meV and 0.2°/0.2° at ALS/DLS, respectively. The fresh surface of single crystals for ARPES measurement was obtained by cleaving the sample *in situ* along its natural (001) cleavage plane.

***Ab initio* calculations:**

Electronic structures were calculated by the density-functional theory (DFT) method which is implemented in the Vienna *ab initio* Simulation Package (VASP). The exchange-correlation was considered in the generalized gradient approximation (GGA) and spin-orbital coupling (SOC) was included self-consistently. Experimental lattice parameters were used in the construction of a slab model with seven-unit-cell thick to simulate a surface, in which the top and bottom surfaces are terminated by P/As and Ta/Nb, respectively. The surface band structures and Fermi surfaces were projected to the top unit cell of the P/As-terminated side,

which fits the experimental band structure well. We adopted a dense k-point grid of 400×400 in Fermi surface calculations.

References and notes:

1 Qi, X.-L. & Zhang, S.-C. Topological insulators and superconductors. *Reviews of Modern Physics* **83**, 1057-1110 (2011).

2 Kong, D. & Cui, Y. Opportunities in chemistry and materials science for topological insulators and their nanostructures. *Nat Chem* **3**, 845-849 (2011).

3 Wan, X., Turner, A. M., Vishwanath, A. & Savrasov, S. Y. Topological semimetal and Fermi-arc surface states in the electronic structure of pyrochlore iridates. *Physical Review B* **83**, 205101 (2011).

4 Xu, G., Weng, H., Wang, Z., Dai, X. & Fang, Z. Chern Semimetal and the Quantized Anomalous Hall Effect in $HgCr_2Se_4$. *Physical Review Letters* **107**, 186806 (2011).

5 Weng, H., Fang, C., Fang, Z., Bernevig, A. & Dai, X. Weyl semimetal phase in non-centrosymmetric transition-metal monophosphides. *Phys. Rev. X* **5**, 011029 (2015).

6 Huang, S.-M. *et al.* A Weyl Fermion semimetal with surface Fermi arcs in the transition metal monopnictide TaAs class. *Nat. Commun.*, 6:7373 (2015).

7 Chenglong Zhang, *et al.* Observation of the Adler-Bell-Jackiw chiral anomaly in a Weyl semimetal. Preprint at http://arxiv.org/abs/1503.02630 (2015).

8 Shekhar, C. *et al.* Extremely large magnetoresistance and ultrahigh mobility in the topological Weyl semimetal NbP. *Nat. Phys.,* 11, 645–649 (2015).

9 Huang, X. *et al.* Observation of the chiral anomaly induced negative magneto-resistance in 3D Weyl semi-metal TaAs. Preprint at http://arxiv.org/abs/1503.01304 (2015).

10 Ghimire, N. J. *et al.* Magnetotransport of single crystalline NbAs. *Journal of Physics: Condensed Matter* **27**, 152201 (2015).

11 Yang, K.-Y., Lu, Y.-M. & Ran, Y. Quantum Hall effects in a Weyl semimetal: Possible application in pyrochlore iridates. *Physical Review B* **84**, 075129 (2011).

12 Zyuzin, A. A. & Burkov, A. A. Topological response in Weyl semimetals and the chiral anomaly. *Physical Review B* **86**, 115133 (2012).

13 Hosur, P. & Qi, X. Recent developments in transport phenomena in Weyl semimetals. *Comptes Rendus Physique* **14**, 857-870 (2013).

14 Balents, L. Weyl electrons kiss. *Physics* **4**, 36 (2011).

15 Liu, C.-X., Ye, P. & Qi, X.-L. Chiral gauge field and axial anomaly in a Weyl semimetal. *Physical Review B* **87**, 235306 (2013).

16 Landsteiner, K. Anomalous transport of Weyl fermions in Weyl semimetals. *Physical Review B* **89**, 075124 (2014).

17 Potter, A. C., Kimchi, I. & Vishwanath, A. Quantum oscillations from surface Fermi arcs in Weyl and Dirac semimetals. *Nat. Commun.* **5**, 6161 (2014).

18 Hosur, P. Friedel oscillations due to Fermi arcs in Weyl semimetals. *Physical Review B* **86**, 195102 (2012).

19 Wang, Z. *et al.* Dirac semimetal and topological phase transitions in A_3Bi (A=Na, K, Rb). *Physical Review B* **85**, 195320 (2012).

20 Liu, Z. K. *et al.* Discovery of a Three-Dimensional Topological Dirac Semimetal, Na_3Bi. *Science* **343**, 864-867 (2014).

21 Liu, Z. K. *et al.* A stable three-dimensional topological Dirac semimetal Cd_3As_2. *Nat. Mater.* **13**, 677-681 (2014).

22 Neupane, M. *et al.* Observation of a three-dimensional topological Dirac semimetal phase in high-mobility Cd_3As_2. *Nat. Commun.* **5**, 4786 (2014).

23 Burkov, A. A. & Balents, L. Weyl Semimetal in a Topological Insulator Multilayer. *Physical Review Letters* **107**, 127205 (2011).

24 Halász, G. B. & Balents, L. Time-reversal invariant realization of the Weyl semimetal phase. *Physical Review B* **85**, 035103 (2012).

25 Xu, S.-Y. *et al.* Experimental realization of a topological Weyl semimetal phase with Fermi arc surface states in TaAs. Preprint at http://arxiv.org/abs/1502.03807 (2015).

26 Lv, B. Q. *et al.* Discovery of Weyl semimetal TaAs. *Phys. Rev. X* 5, 031013 (2015).

27 Xu, J. *et al.* Crystal Structure, Electrical Transport, and Magnetic Properties of Niobium Monophosphide. *Inorganic Chemistry* **35**, 845-849 (1996).

28 Chen, Y. Studies on the electronic structures of three-dimensional topological insulators by angle resolved photoemission spectroscopy. *Front. Phys.* **7**, 175-192 (2012).

Acknowledgements:

Y.L.C acknowledges the support from the EPSRC (UK) grant EP/K04074X/1 and a DARPA (US) MESO project (no. N66001-11-1-4105). C.F. and B.Y. acknowledge that the financial supported by the Deutsche Forschungsgemeinschaft DFG (Project No.EB 518/1-1 of DFG-SPP 1666 "Topological Insulators") and by the ERC Advanced Grant (No. 291472 "Idea Heusler"). Advanced Light Source is operated by Department of Energy, Office of Basic Energy Science (contract DE-AC02-05CH11231).

Author Contributions:

Y.L.C conceived the experiments. Z. K. L and L. X. Y carried out ARPES measurements with the assistance of T. Z, H. P, H. F. Y, C. C, Y. Z and S. K. M, D.P, M.S and Y.F.G synthesized and characterized the bulk single crystals. B.H.Y and Y.S. performed *ab initio* calculations. All authors contributed to the scientific planning and discussions.

Competing financial interests:

The authors declare no competing financial interests.

Figure 1. Properties of TWSs and characterization of NbP/TaP single crystals.

a, Schematic of bulk and (001) surface Brillouin zones (BZs) of transition metal monopnictides. Twelve pairs of Weyl points predicted by theoretical investigations[5,6] (see text for details) are marked as red and blue dots. **b,** Illustration of the separation of a pair of Weyl points (with opposite chirality, marked as WP+ and WP-) controlled by the SOC strength in different compounds of the family. The dotted line represents the crystalline mirror plane, and the grey arcs represent the surface Fermi-arcs that connect the two Weyl points. **c.** *Ab initio* calculations show the Weyl points and surface Fermi-arcs of NbP, TaP and TaAs, respectively. The color bar shows the surface contribution of the FS (white/0% to red/100%), same for Fig. 2-4. **d,** Crystal structure of NbP/TaP, showing the ..A-B-C-D… stacking of NbP/TaP layers. Red arrows indicate interlayer positions where cleavage possibly takes place. **e, (i)** Image of NbP single crystals with shining flat surface used for ARPES measurements. **(ii-iv)** X-ray diffraction patterns from (100), (001) and (010) directions. **f,** Core level photoemission spectrum of NbP shows characteristic Nb (*4s, 4p, 3d*) and P (*2s, 2p*) peaks. **g,** Broad FS mapping of NbP shows excellent agreement with the *ab initio* calculations (overlapped red dotted plots). The orthogonal spoon-like and bowtie-like FS pockets are denoted as α- and β- FSs, respectively, same in **h**. Blue color bar indicates the ARPES spectra intensity, same for Fig. 2-4. **h,** Broad FS mapping of NbP from two adjacent cleaved NbP

layers shows the mixing of two sets of electronic structure rotated by 90 degrees from each other.

Figure 2. Overall electronic structure of NbP.

a, Stacking plots of constant-energy contours at different binding energies showing the band structure evolution. Red square marks the first BZ. **b,** Side-by-side comparison of three constant energy contours between experiments (left panels) and *ab initio* calculations (right panels) shows overall agreements. **c,** 3D intensity plots of the photoemission spectra around the $\bar{X}$ (i) and $\bar{Y}$ (ii) points illustrate the zoomed-in band structure for both the bowtie- and spoon-like FSs with overlaid dispersions from calculation. **d,** Comparison of calculated (i) and experimental (ii) dispersions along high symmetry directions across the whole BZ ($\bar{M} - \bar{X} - \bar{\Gamma} - \bar{Y} - \bar{M}$). **e,** Plot of photoemission intensities at E_F along the high symmetry $\bar{Y} - \bar{\Gamma} - \bar{Y}$ direction (measurement position is along the green line marked on the FS in the lower panel) as a function of photon energy (82-130eV), showing the k_z dispersion of different bands.

Figure 3. Overall electronic structure of TaP.

a, Stacking plots of constant-energy contours of the full BZ at different binding energies showing the band structure evolution. **b,** Comparison of three constant energy contours at different binding energies between experiments (left panels) and *ab initio* calculations (right panels) shows excellent agreements. **c,** 3D intensity plots of the photoemission spectra around the $\bar{X}$ (i) and $\bar{Y}$ (ii) point illustrate the zoomed-in band structure for both the bowtie- and spoon-like FSs with overlaid dispersions from calculation. **d,** Schematic of an arbitrary reference loop in the momentum space crossing a closed Fermi pocket and a broken Fermi arc. **e,** (i) Comparison of calculated and experimental high symmetry cuts along a closed reference loop in the momentum space ($\bar{M} - \bar{X} - \bar{\Gamma} - \bar{M}$). Green arrows denote the Fermi surface

crossings. (ii) Schematic of the closed reference loop in the momentum space as well as the labelled positions of FS crossings along the loop. Colored dots show the position of the Weyl points in the BZ.

Figure 4. Evolution of the band structure with SOC.

a, (i) Schematic plot shows a pair of Weyl points projected to the (001) surface BZ and the Fermi-arc connecting them. (ii-iv) Comparison of the calculated and ARPES measurement of the spoon-like FSs, showing nice agreement. Red/blue dots denote the Weyl points of opposite chirality (labelled as WP+ and WP-). **b-d,** High resolution ARPES measurements on the spoon-like FS (i) and associated band dispersions (ii-iii) for NbP, TaP and TaAs, respectively. The positions of the band dispersions presented in (ii-iii) are indicated by the red dotted lines in (i). $\Delta K1$ and $\Delta K2$ represent the separation between the Weyl points and Fermi arcs, respectively. **e,** Summary of the extracted $\Delta K1$ and $\Delta K2$ (from **b-d**) from three compounds, plotted against the SOC strength.

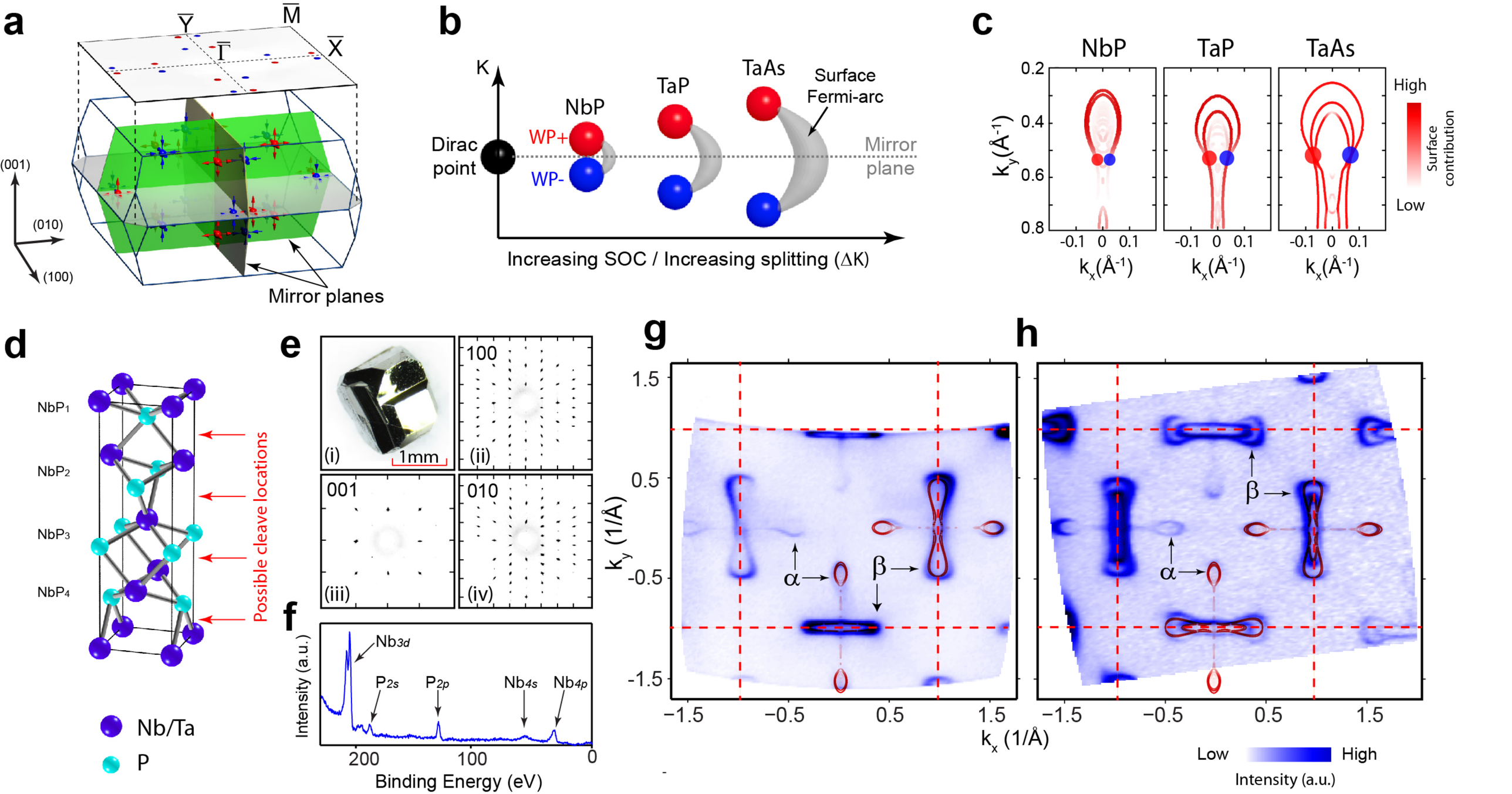
a
Y
M
Γ
X
(001)
(010)
(100)
Mirror planes
b
K
NbP
TaP
TaAs
Surface
Fermi-arc
Dirac
point
WP+
WP-
Mirror
plane
Increasing SOC / Increasing splitting (ΔK)
c
NbP
TaP
TaAs
0.2
0.4
0.6
0.8
k_y(Å^{-1})
-0.1 0 0.1
k_x(Å^{-1})
High
Low
Surface
contribution
d
NbP1
NbP2
NbP3
NbP4
Possible cleave locations
Nb/Ta
P
e
(i)
1mm
100
(ii)
001
(iii)
010
(iv)
f
Intensity (a.u.)
Nb3d
P2s
P2p
Nb4s
Nb4p
200
100
0
Binding Energy (eV)
g
h
1.5
0.5
-0.5
-1.5
k_y (1/Å)
α
β
−1.5 −0.5 0.5 1.5
k_x (1/Å)
Low
High
Intensity (a.u.)

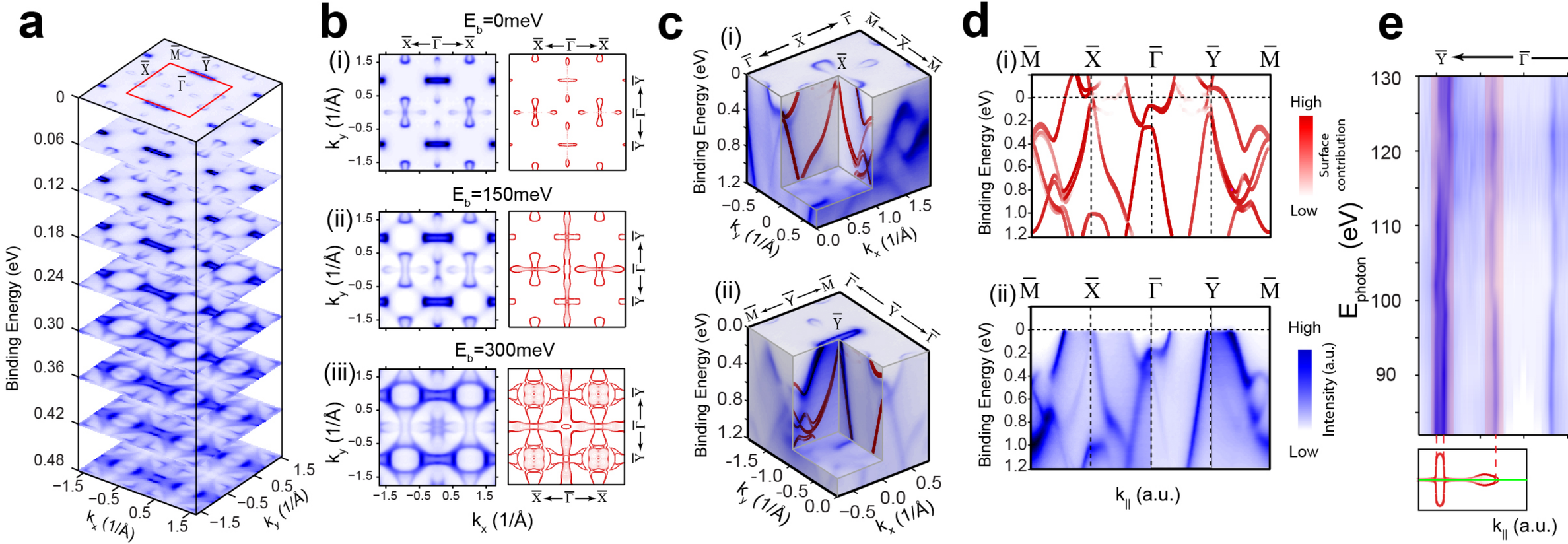
a
b
c
d
e
Binding Energy (eV)
k_x (1/Å)
k_y (1/Å)
E_b=0meV
E_b=150meV
E_b=300meV
$\bar{X}$
$\bar{M}$
$\bar{Y}$
$\bar{\Gamma}$
High
Low
Surface contribution
Intensity (a.u.)
$k_{||}$ (a.u.)
E_{photon} (eV)

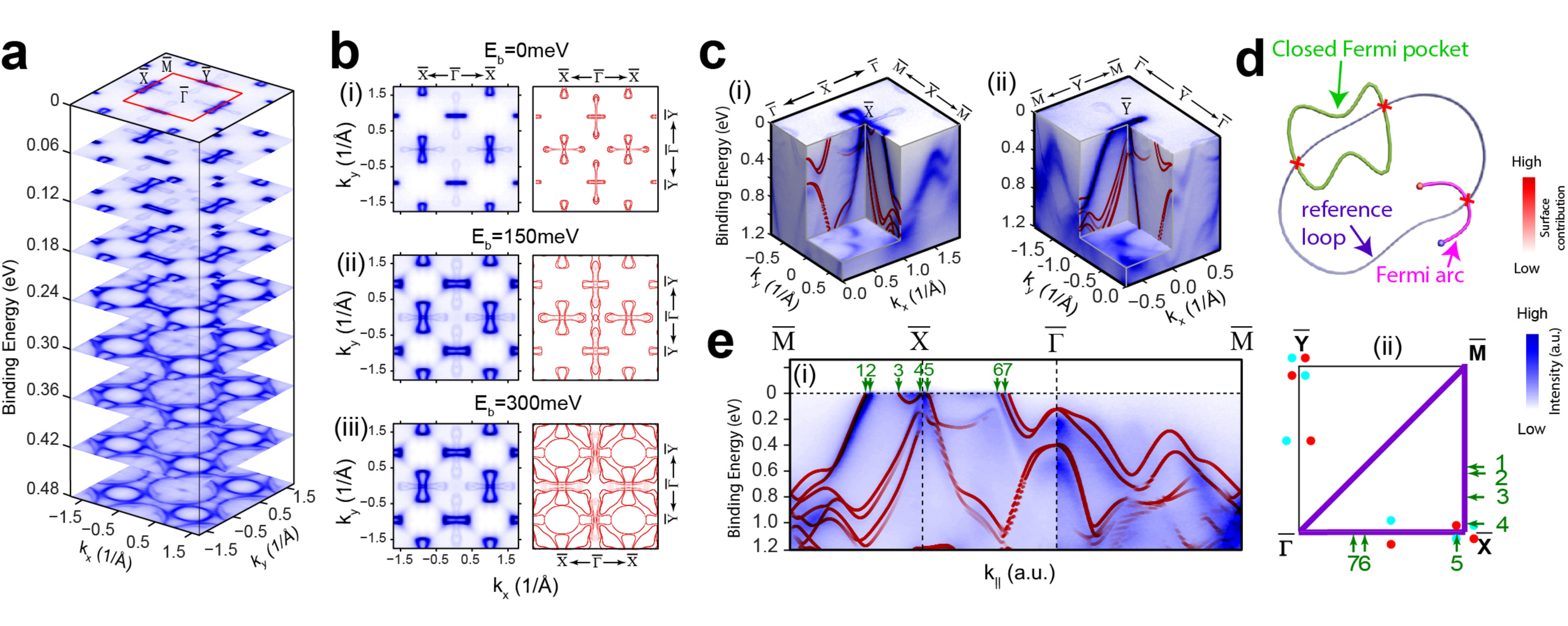
a
b
c
d
e
Binding Energy (eV)
k_x (1/Å)
k_y (1/Å)
E_b=0meV
E_b=150meV
E_b=300meV
Closed Fermi pocket
reference loop
Fermi arc
High
Low
Surface contribution
Intensity (a.u.)
$k_{||}$ (a.u.)

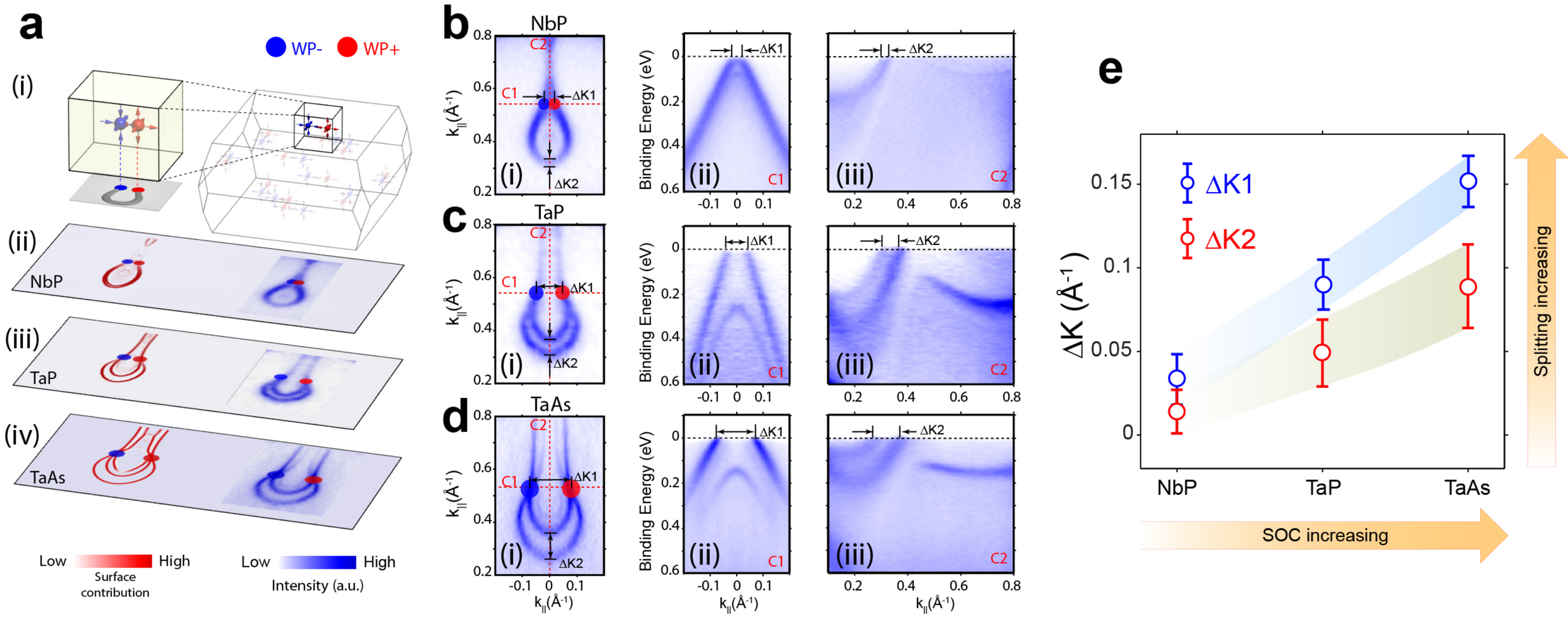
a
WP-
WP+
(i)
(ii)
NbP
(iii)
TaP
(iv)
TaAs
Low
High
Surface contribution
Low
High
Intensity (a.u.)
b
NbP
c
TaP
d
TaAs
C1
C2
ΔK1
ΔK2
(i)
(ii)
(iii)
$k_{||}$(Å^{-1})
Binding Energy (eV)
e
ΔK (Å^{-1})
ΔK1
ΔK2
NbP
TaP
TaAs
SOC increasing
Splitting increasing